



Multi-viewpoint Coronal Mass Ejection Catalog Based on *STEREO* COR2 Observations

Angelos Vourlidas^{1,4}, Laura A. Balmaceda^{2,5,6}, Guillermo Stenborg³, and Alisson Dal Lago²¹The Johns Hopkins University Applied Physics Laboratory, Laurel, MD, USA²National Institute for Space Research (INPE) 12227 São José dos Campos, SP, Brazil³Space Science Division, US Naval Research Laboratory, Washington, DC, USA

Received 2017 February 14; revised 2017 March 13; accepted 2017 March 15; published 2017 April 4

Abstract

We present the first multi-viewpoint coronal mass ejection (CME) catalog. The events are identified visually in simultaneous total brightness observations from the twin SECCHI/COR2 coronagraphs on board the *Solar Terrestrial Relations Observatory* mission. The Multi-View CME Catalog differs from past catalogs in three key aspects: (1) all events between the two viewpoints are cross-linked, (2) each event is assigned a physics-motivated morphological classification (e.g., jet, wave, and flux rope), and (3) kinematic and geometric information is extracted semi-automatically via a supervised image segmentation algorithm. The database extends from the beginning of the COR2 synoptic program (2007 March) to the end of dual-viewpoint observations (2014 September). It contains 4473 unique events with 3358 events identified in both COR2s. Kinematic properties exist currently for 1747 events (26% of COR2-A events and 17% of COR2-B events). We examine several issues, made possible by this cross-linked CME database, including the role of projection on the perceived morphology of events, the missing CME rate, the existence of cool material in CMEs, the solar cycle dependence on CME rate, speeds and width, and the existence of flux rope within CMEs. We discuss the implications for past single-viewpoint studies and for Space Weather research. The database is publicly available on the web including all available measurements. We hope that it will become a useful resource for the community.

Key words: catalogs – Sun: activity – Sun: coronal mass ejections (CMEs) – techniques: image processing

1. Introduction

Long-running space missions dedicated to the continuous observing of the solar corona have enabled the systematic study of transient coronal phenomena, such as coronal mass ejections (CMEs). Consequently, several catalogs listing their kinematic and dynamical characteristics have been compiled since the 1970s. Currently, most CME catalogs are based on the images from the Large Angle and Spectrometric Coronagraphs experiment (LASCO; Brueckner et al. 1995), which has been observing coronal activity for more than 20 years on board the *Solar and Heliospheric Observatory* (*SOHO*, Domingo et al. 1995). With the advent of the *Solar Terrestrial Relations Observatory* (*STEREO*, Kaiser et al. 2008) mission several efforts were also made to adapt the methodologies devised for LASCO to the white light imagery from the Sun Earth Connection Coronal and Heliospheric Investigation (SECCHI, Howard et al. 2008) suite on board the twin *STEREO* spacecraft.

Event catalogs offer several benefits to researchers: (1) they simplify access to the data by identifying and categorizing events for further study; (2) they allow assessment of interesting trends, e.g., event rates, periods of low/high activity; and (3) the accompanying measurements provide insights into the CME phenomenon, i.e., solar cycle variation of speed, mass, energy, etc.

Based on their compilation method, event catalogs can be split into manual and automated catalogs. Manual catalogs are built by humans making both the event identification and the

various measurements (e.g., speed, position angle, width). Examples of manually produced catalogs are the *SOHO*/LASCO catalog⁷ (Yashiro et al. 2004; Gopalswamy et al. 2009, 2010) and the *STEREO*/COR1 preliminary list,⁸ though the latter provides only CME identifications and not measurements of their properties. Manually produced catalogs are obviously subjective. “Observer bias” is a common criticism levied against manually produced catalogs as the identification of events and the selection of their boundaries, leading edge, and other properties is subject to the observer’s experience, concentration, and preconceived ideas. Moreover, the manual measurements can become tedious and time consuming, especially during high activity periods and/or high cadence observations, which may decrease the measurement reliability and may result in fewer measurements per event. On the other hand, experience operators bringing their insights in event detection and boundary selection, are able to identify wide, faint events and separate overlapping events during high activity periods.

To overcome the inherent subjectivity of manual catalogs, several automated methods have been devised and deployed to detect and track CMEs. Examples of such catalogs include CACTus⁹ (Computer Aided CME Tracking; Berghmans 2002; Robbrecht & Berghmans 2004; Robbrecht et al. 2009; Bonte et al. 2011) SEEDS¹⁰ (Solar Eruptive Events Detection System; Olmedo et al. 2008); ARTEMIS I and II¹¹ (Automatic Recognition of Transient Events and Marseilles Inventory from Synoptic maps; Boursier et al. 2009; Floyd et al. 2013; Boursier et al.

⁴ Also at IAASARS, National Observatory of Athens, GR-15236, Penteli, Greece.

⁵ National Council for Scientific and Technological Research, CONICET, Argentina.

⁶ Now at George Mason University, Fairfax, VA, USA.

⁷ http://cdaw.gsfc.nasa.gov/CME_list/index.html

⁸ <http://cor1.gsfc.nasa.gov/catalog/>

⁹ <http://sidc.oma.be/cactus/>

¹⁰ <http://spaceweather.gmu.edu/seeds/>

¹¹ <http://cesam.lam.fr/lascommission/ARTEMIS/>

2005); and CORIMP¹² (Coronal Image Processing; Byrne et al. 2012). These catalogs were initially designed to detect CMEs in LASCO data, but CACTus¹³ and SEEDS have been adapted for STEREO/COR2 data. Another technique, using observations from all three coronagraph viewpoints, was introduced recently by Hutton & Morgan (2017). Their Automated CME Triangulation (ACT) algorithm looks promising but it is validated with a very small sample of observations so its advantages and constraints remain unclear for the moment. The detection algorithms differ in many ways including (1) the image processing technique performed on the data before segmentation, (2) the image representation on which the segmentation is performed (e.g., synoptic maps, polar or Cartesian representation of the image, height–time maps, etc.), and (3) the mathematical property or criteria used to segment the feature of interest. In contrast to the manual methods, automated methodologies provide observer-independent measurements, are more capable of handling large amounts of data, and are faster. However, automated catalogs suffer from significant biases. Their event detectability depends on the choice of the threshold to represent the undisturbed corona. That choice depends on the solar cycle phase, the level of solar activity, the number of foreground and background structure, etc. It cannot be reliably set automatically. The background level also affects the visibility (and hence detectability) of the CME front and boundaries. High activity levels confuse automated algorithms, which miss events or cannot identify their boundaries. Faint events, such as events out of the sky plane (halo-CMEs) or events during solar minimum are especially hard to detect automatically. Recently, Hess & Colaninno (2017) demonstrated that observation cadence is another concern because it can affect both the detection of CMEs and the physical properties extracted by automated methods. In particular, the unreliability of halo-CME detection by automated algorithms is the single largest impediment in their use in operational space weather settings.

Therefore, manual and automated CME lists are subject to (different) biases. However, they all share a common limitation. They suffer from projection effects because all catalogs are based on observations from a single-viewpoint—along the Sun–Earth line, in the case of LASCO. Past literature has discussed how projection affects CME kinematics (Burkepile et al. 2004; Temmer et al. 2009; Shen et al. 2013), energetics (Vourlidas et al. 2010), and event detectability, size, and morphology (Vourlidas et al. 2013; Kwon et al. 2015). In a nutshell, projection effects lead to both underestimation (for nearly-planar structures, such as streamer blobs) and overestimation of CMEs sizes (for more circular structures, such as three-part CMEs) of CME sizes, underestimation of CME speeds, masses and energies, and under-reporting of very narrow and wide, but faint, CMEs.

The large amount of multi-viewpoint data accumulated during the 10 years of *STEREO* operations provides a great opportunity to create a CME database free (or largely free) from projection effects and to assess the reliability of past single-viewpoint measurements in view of projection effects. The first dual-viewpoint CME catalog¹⁴ based on SECCHI/COR2 observations from 2007 to 2011 was compiled by Bosman et al. (2012) at the Institute for Astrophysics Göttingen (IAG). The IAG catalog contains 1060 events and reports the date/time, position angle, and other viewing geometry information for each CME in

both COR2 telescopes. Additionally, a subset of 263 events, so-called “Best of” CMEs because of their clear structure, are also identified in LASCO. Finally, 243 of these events are reconstructed using forward modeling (Thernisien 2011), for a single time only, and their 3D parameters cataloged. Initial results are discussed in Bosman et al. (2012). The IAG catalog is the most comprehensive multi-viewpoint CME catalog to date.

Here, we take the obvious next step and build the full dual-viewpoint COR2 CME catalog. We name it, the Multi-View CME (MVC) catalog because we plan to add the LASCO viewpoint in the near future. Our work differs from the IAG catalog in several important ways. It provides morphological classification for each event, adds kinematic and size information, and extends the catalog to the end of dual COR2 observations in 2014 September. In addition, we introduce a “hybrid” approach in building the catalog. We use the advantages of both manual and automated methods; namely, manual identification and classification of CMEs, which overcomes issues with overlapping or faint events and automation of the measurements, which offers speed and a larger number of data points. The MVC catalog available online¹⁵ provides the first statistically significant collection of simultaneous multi-viewpoint measurements of CME events over the full range of viewing angles (0–180°) and the largest sample of CMEs classified by morphology. We hope that it is a valuable resource for the Heliophysics community and that it will assist in numerous investigations.

The paper is structured as follows. In Section 2, we outline the methodology for the compilation of the event list and their morphological classification. In Section 2.2, we explain how the measurements are carried out by using a novel supervised technique. In Section 3, we present the first results from the analysis of the CME morphology (Sections 3.1–4.3) and of their kinematic properties (Section 3.2) from multiple viewing angles. We discuss the implications in Section 4 and conclude in Section 5.

2. Methodology

To create the MVC catalog, we employ a three-stage procedure. The first stage consists of the manual identification and classification of a CME in both COR2 telescopes and produces the cross-linked CME list. The second stage takes as input the cross-linked CME list and proceeds to isolate the event from the background and track it through the COR2 field of view (FOV). The procedure employs a supervised computer vision algorithm, called CORSET (CORonal SEGmentation Technique; Goussies et al. 2010), described in Section 2.2. The third stage consists of extracting and organizing the morphological and kinematic properties of the events using customized software routines.

2.1. The Cross-linked CME List: Manual Identification and Classification of Events

The CME list is based on the white light total brightness images from the COR2 coronagraphs obtained between 2007 March and 2014 September. The COR2 images (2048 × 2048 pixels) are recorded with the nominal 15 minute cadence during most of this period, and their FOV extends from 2.5 to 15 R_{\odot} (15 arcsec pixel⁻¹ plates scale).

¹² <http://alshamess.ifa.hawaii.edu/CORIMP/>

¹³ <http://secchi.nrl.navy.mil/cactus/>

¹⁴ <http://www.affects-fp7.eu/cme-database/>

¹⁵ <http://solar.jhuapl.edu/Data-Products/COR-CME-Catalog.php>

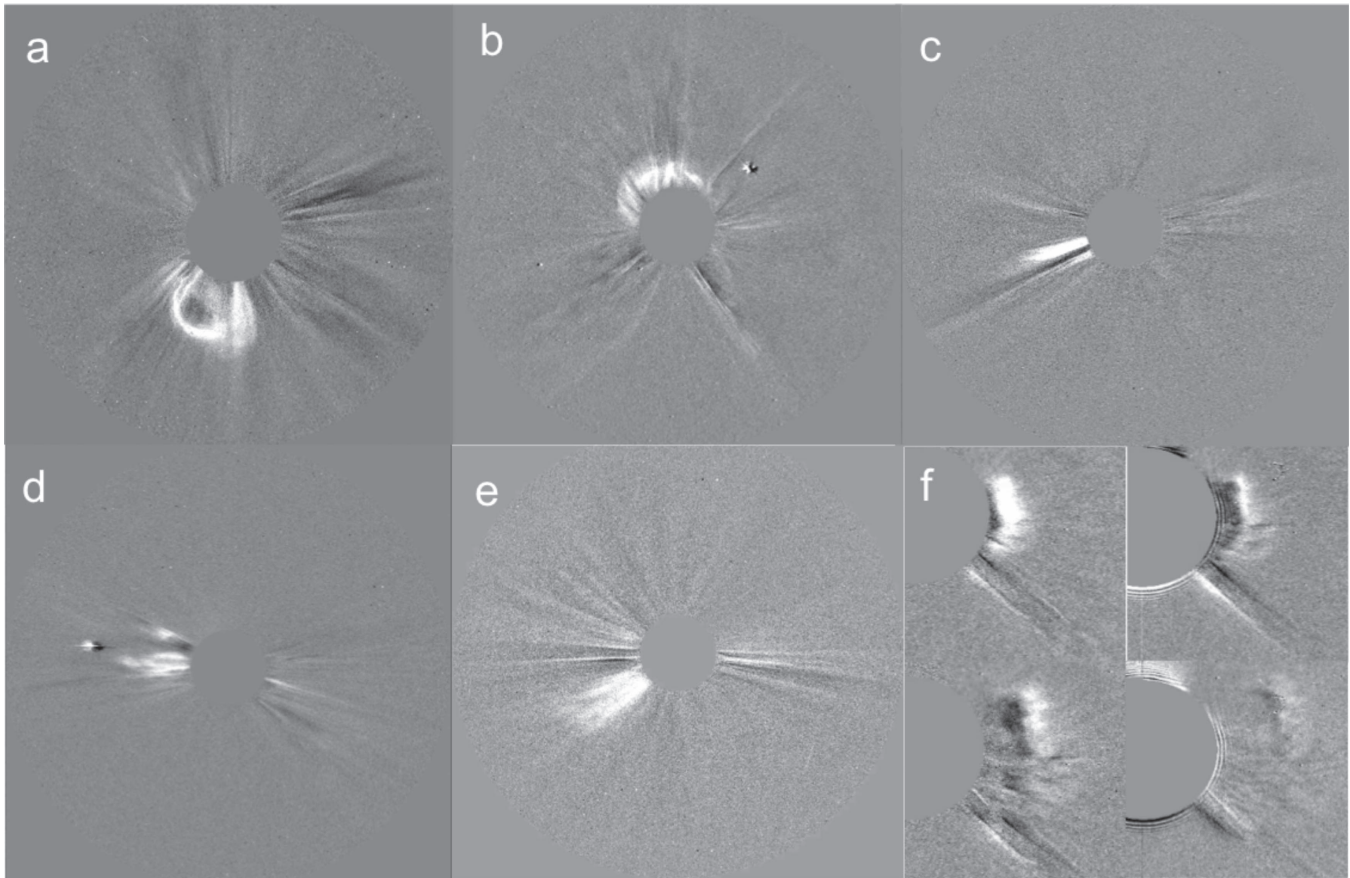


Figure 1. Base-difference images illustrating the CME morphological classes used in the event catalog. (a) Flux-rope, (b) Loop, (c) Jet, (d) Other, (e) Unknown, and (f) Wave, showing a four-image sequence.

The events are recorded in separate lists for COR2-A and -B, but the identifications are done by simultaneous viewing of both telescopes’ time series. Given the desired start date, our software reads the COR2-A and B image files from the archive, divides the images by a background image, and plays the resulting quick-look movies side-by-side on the screen. The user can advance forward or backward in time with the keyboard and switch the display to running or base-difference movies on-the-fly. Once an event is identified in at least one of the telescopes, the user begins to record basic information: (1) the pre-event time and the times of the images where the event is fully visible in the given coronagraph FOV (this information will be used to derive the mass and energetics of each event in a later phase of the project), (2) a morphological classification of the event (see below for details), and (3) the quadrant occupied by the event. Each event is assigned a unique identifier (ID), which is identical when the same event is observed in the other telescope with the same onset time. The list is compiled by two observers only (LB and AV).

The criteria behind the morphological classification of CMEs have been discussed in detail in Vourlidas et al. (2013) for LASCO CMEs. They classified CMEs into several morphological categories based on their appearance at $\sim 10 R_{\odot}$ or higher, where their morphology becomes clear. In the present study, we adopt the Vourlidas et al. (2013) definitions as follows (a representative image for each type is shown in Figure 1).

1. *Flux Rope (F)*: CMEs exhibiting either a three-part morphology (i.e., a circular front, cavity, and bright core)

or a clear front followed by a cavity but lacking the core (Figure 1(a)).

2. *Loop (L)*: We follow the definition given in Vourlidas et al. (2013), i.e., “CMEs with a bright, filamentary loop-like appearance lacking a cavity and/or a core” (Figure 1(b)). These events, discussed extensively in Vourlidas et al. (2013), are F-CMEs with their axis projected face-on on the sky plane. See also Figure 15 in Cremades & Bothmer (2004).
3. *Jet (J)*: We follow the definition given in Vourlidas et al. (2013), i.e., “CMEs with angular width $< 40^{\circ}$ lacking a sharp front, detailed sub-structure, or circular morphology” (Figure 1(c)).
4. *Other (O)*: Mass ejections, wider than jets but lacking clear signatures of flux ropes or loops so they cannot be categorized in any of the other classes with confidence. Some have a cloud-like appearance (Figure 1(d)) and many look like, and may originate from, $H\alpha$ surges, as for example the event analyzed by Vourlidas et al. (2003; their Figure 1).
5. *Unknown (U)*: This category mostly includes events that are either very faint or suffer from poor observations (e.g., overlapping with other events, excessive presence of cosmic rays, data dropouts, etc.). They may be as large as regular CMEs and may contain filamentary material (Figure 1(e)). Because they are poorly observed events, we do not consider them to be CMEs in our analysis here.
6. *Wave-like (W)*: Events exhibiting fronts that fade away as they cross the coronagraph FOV in spite of being bright

Table 1
Alphabetical List of Keywords used in Providing Further Details
for Each Event

| Keyword | Explanation |
|---------|--|
| 3P | 3-part structure CME |
| CS | “Current sheet” or post-CME ray |
| COL | Possible collision with previous CME |
| DFL | Likely deflection of the event within the FOV |
| DPL | CME exhibits dimpled front |
| Faint | Faint event; may affect type assignment |
| FF | Event fails/disappears before exiting COR2 FOV |
| Front | Bright front; may be evidence of pileup |
| Gap | Data gap |
| Ha | Bright emission (likely H-alpha emission) |
| HAL | Halo CME |
| KEY | Keyhole-hole shaped CME |
| OFL | Outflowing material at the back of the CME |
| OVR | Event partially overlaps with another CME |
| PRM | Prominence material (filamentary structures) |
| SB | Streamer Blowout following CME |
| SEP | Solar Energetic Particle event |
| SLB | Side-lobe Operations |
| SUR | Surge-like eruption |

enough during their early development (Figure 1(f)). They often consist of successive fronts showing the appearance of ripples on the background scene (a possible example is in Alzate & Morgan 2016). The so-called “failed CMEs” (Vourlidas et al. 2010) belong to this group. These events are highly unlikely to be CMEs.

7. *Shock candidate (S)*: This keyword is used to note whether a faint front exists beyond the CME front that could be a shock or wave driven by the event (Vourlidas et al. 2013). It is used in *addition* to the standard classification above (e.g., “FS” or “SO,” etc.). We do not discuss these cases here.

We take great care to perform the CME classification independently for each telescope so we can investigate how the viewpoint affects the CME appearance with very interesting results (Section 3.1). The description for each event is enhanced with remarks, described via standardized keywords (to facilitate search operations), which provide details on aspects such as (i) morphology and appearance, e.g., halo CME, streamer blowout events, three-part structure, bright front, failed CMEs; (ii) CME-related phenomena, e.g., prominence material, outflows, post-CME rays; (iii) CME-dynamics, e.g., deflection, collision. Finally, the entry is completed with comments that describe observational issues that may influence the interpretation, e.g., overlapping events, presence of energetic particles, data gaps, etc. The complete list of the keywords and a short explanation is given in Table 1

2.2. CME Detection and Tracking Using a Supervised Computer Vision Algorithm

We employ a supervised computer vision technique to track and measure the CME events, identified visually in the CME lists. The CORSET algorithm (Goussies et al. 2010) is specifically developed for white light coronagraphic observations. It is designed to separate from the underlying background corona and track discrete, outgoing white light coronal features via a texture-based segmentation procedure. CORSET is a

supervised technique because it requires a user to roughly outline the CME region in a single coronagraph frame, usually when the event first appears.

We apply CORSET on COR2 total brightness background ratio or quick-look images, i.e., solar north up, bias correction, but no corrections for instrument response, stray light, etc. The background image is the monthly minimum image. Briefly, the supervised stage consists of the manual selection of two regions of interest (ROI), one comprising the CME feature and another containing a sample of the background, in the ratio image when the CME first appears in the FOV. The base image is simply a pre-event image, close enough in time to account for the pseudo-static features. The two ROIs are used by the algorithm to compute the initial texture characteristics (i.e., the spatial distribution of the gray levels of the pixels) of both the CME and the background.

The initial, user-defined CME region is evolved by the algorithm by comparing its texture to that of the background. Once the CME feature is segmented, the algorithm uses this result as the CME region initial guess for the following time frame. The detection procedure is repeated throughout the sequence of images. The reader is referred to Goussies et al. (2010) for the detailed mathematical procedure and formalism.

2.3. Automatic Determination of the CME Geometric, Kinematic, and Dynamical Properties

After a CME is detected and tracked by CORSET, we use a set of tools, adopted from Goussies et al. (2010) and Braga et al. (2013), to automatically extract its morphological, kinematic, and dynamical properties. Since CORSET detects the CME outer boundary, it provides the locations of all the pixels across that boundary. From that information, we compute the following quantities for each frame: (1) the heliocentric heights of the CME outer boundary, (2) its central position angle (CPA), measured counterclockwise from solar north, defined as the midpoint between the position angles of the two flanks of the CME, and (3) the angular width (computed as the angular difference of the CME flanks). From all the images for a CME, we then calculate the radial speed at a given user-defined position angle (see below), the expansion speed, the position angle of the maximum instantaneous speed (MPA), and the speed as a function of the position angle along the CME boundary. All of these values are stored in separate files within the online data directory for each event.

To characterize each event and to maintain a similar structure to the LASCO CME catalog (which most of the community is familiar with), we derive a single value for these metrics as follows. (1) The event CPA is the median of the CPAs derived in each time frame, (2) similarly, the width is the median of the values from all frames, and (3) the radial and expansion speeds (linear, second order at $10 R_{\odot}$) are computed along the CPA. These values are then stored in the corresponding database for the given COR2 telescope and are reported as the “representative” values for that event.

As an example, we show in Figure 2 some of the geometric and kinematic properties of the 2010 April 3 CME. The top middle panel shows the CME outer boundary contour (black line) identified by CORSET at 11:24 UT. The bottom middle panel shows the CME segmentation for each frame in the time sequence analyzed (the temporal evolution is represented by the different gray levels). The straight line represents the CPA. In the top left (COR2-B) and right (COR2-A) panels of

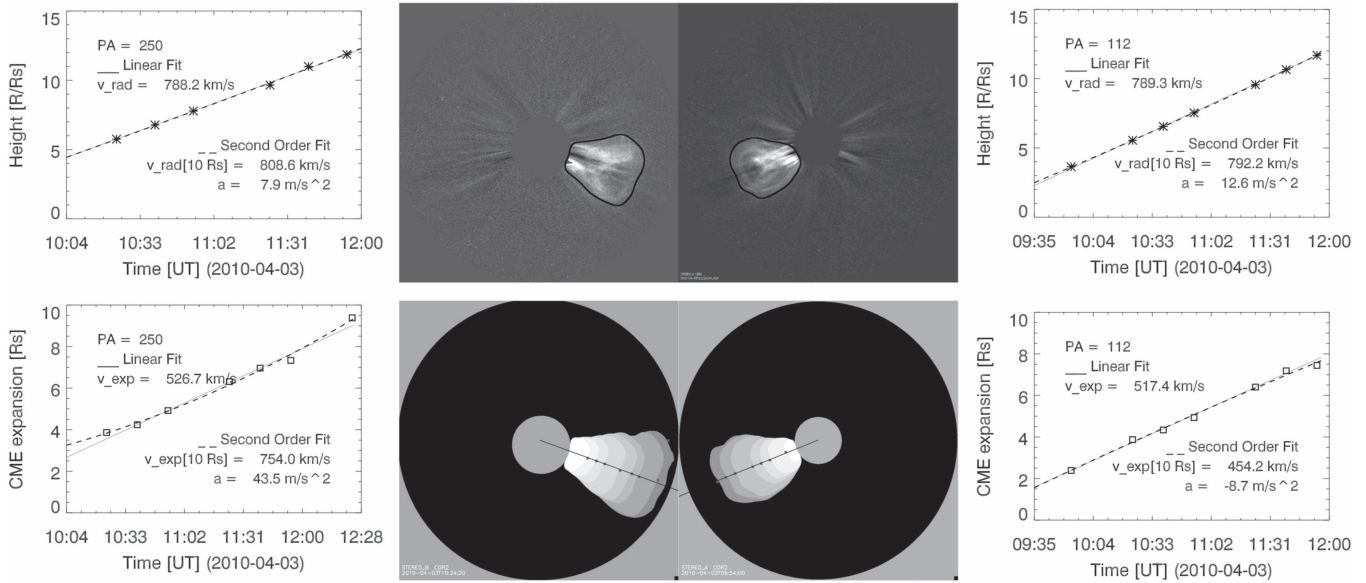


Figure 2. Left column: COR2-B radial height–time plot and speed estimates (top), and angular width–time plot and expansion speed estimates (bottom) for the CME on 2010 April 3. Right column: the same quantities for COR2-A images.

Figure 2, we indicate the location of the CME leading edge along the CPA, as detected by CORSET. From these height–time (HT) plots, the CME speed is derived by fitting either a constant speed, or a constant acceleration model. For the second case, we list the speed at $10 R_{\odot}$. Our software can also derive the CME front speed (and acceleration) along radial lines spanning the CME angular width at 1° position angle intervals, but these measurements are not presented here. Note that all of these quantities are projected quantities on the given telescopes’ sky plane. In the bottom left and right panels of Figure 2, we show plots of the lateral expansion (in R_{\odot}) of the CME. The lateral spread is derived at the location, where the distance perpendicular to the direction of propagation is the greatest. The expansion speed of the CME is determined simply by fitting a linear model (constant speed) or a second-degree polynomial (constant acceleration). As with the radial propagation speed, the expansion speed for the second-degree fit is reported at $10 R_{\odot}$.

3. Results

The CME catalog extends from 2007 March (when regular COR2 observations begin) to 2014 September 27 (the last day of COR2-B observations). As of the time of this writing, the COR2-B entries begin in 2007 May but the gap will be filled in the near future. The catalog contains 4473 unique events (CMEs detected in at least one COR2 telescope). Of these, 3558 events (75% of total) were observed in both COR2-A and B. COR2-A recorded 4262 events (95%) and COR2-B recorded 3769 events (84%). The numbers are not corrected for duty cycle but suggest that COR2-A may be more sensitive than COR2-B given the very similar concept of operations for both spacecraft. In the rest of the section, we discuss the fractional distribution of the CME morphologies (Section 3.1) and present the geometric and kinematic properties of the events successfully tracked by CORSET (Section 3.2).

3.1. CME Morphology Types

Table 2 summarizes the morphological distribution of CMEs per telescope and per year. We indicate the separation angle between the two spacecraft at the bottom. We find that each coronagraph records a very similar fraction of a given CME type, which indicates that (1) the two telescopes are very similar and that (2) any sensitivity differences do not affect the appearance of CME, which is reassuring.

At the bottom of the table, we calculate the yearly fractions of the assumed flux-rope (FR) CMEs (types “F” and “L,” see discussion in Vourlidas et al. 2013). Overall, FR-CMEs comprise about 40% of the total, in close agreement with the LASCO statistics in Vourlidas et al. (2013). However, the number of “L” types in COR2 is much smaller than in LASCO C2. For example, in 2010, there were 56 L-type LASCO CMEs (Table 1, Vourlidas et al. 2013) but only 21 in COR2-B. One possible explanation is the lower signal-to-noise ratio (SNR) in the COR2 images compared to C2, which may reduce the visibility of the loop front and leading us to categorize the CME as an “F” CME. There is a much larger number of “F”-type CMEs in the COR2s (245–267) than in LASCO-C2 (156) for 2010. Another possibility is the weaker Cycle 24. As we demonstrated in Vourlidas et al. (2013), the bright loop arises from pileup of material from the lower corona and is more likely to occur in impulsive CMEs. However, Cycle 24 is characterized by lower activity and lower CME speeds, which, combined with the lower SNR in COR2, leads to fewer L-CME detections.

The yearly percentages of FR-CMEs (row labeled “F+L”) show that their fraction remains relatively constant during the minimum of Cycle 23 through 2010 with a rapid increase to 45%–48% around the peak of cycle 24. The lower numbers in 2014 are due to the switch of *STEREO-A* telemetry to side-lobe downlink in July and the interruption of observations in 2014 September. Also 2007 statistics start in March for COR2-A and May for COR2-B. On the other hand, the total yearly number of CMEs follow the solar cycle evolution, as expected.

Table 2
Distribution of CME According to Morphological Types through the Solar Cycle

| Type | COR2 | 2007 | 2008 | 2009 | 2010 | 2011 | 2012 | 2013 | 2014 | Total | Fraction |
|--------------|------|------|-------|--------|---------|---------|--------|-------|-------|-------|----------|
| F | A | 50 | 35 | 83 | 167 | 267 | 292 | 276 | 195 | 1376 | 32% |
| | B | 31 | 48 | 60 | 141 | 245 | 258 | 254 | 198 | 1235 | 33% |
| L | A | 9 | 6 | 4 | 14 | 55 | 101 | 76 | 52 | 317 | 7% |
| | B | 5 | 7 | 1 | 21 | 58 | 104 | 73 | 50 | 319 | 8% |
| O | A | 42 | 78 | 82 | 178 | 278 | 331 | 318 | 192 | 1499 | 35% |
| | B | 23 | 71 | 70 | 165 | 276 | 285 | 270 | 180 | 1340 | 36% |
| J | A | 35 | 48 | 22 | 58 | 60 | 41 | 24 | 87 | 375 | 9 % |
| | B | 14 | 32 | 12 | 39 | 58 | 33 | 21 | 81 | 290 | 8 % |
| U | A | 24 | 44 | 28 | 54 | 108 | 85 | 113 | 49 | 505 | 12% |
| | B | 16 | 25 | 20 | 48 | 107 | 71 | 95 | 56 | 438 | 12% |
| W | A | 15 | 8 | 2 | 21 | 34 | 26 | 19 | 65 | 190 | 4% |
| | B | 7 | 3 | 3 | 16 | 30 | 9 | 7 | 72 | 147 | 4% |
| Total | A | 175 | 230 | 221 | 492 | 802 | 877 | 828 | 640 | 4262 | |
| | B | 96 | 186 | 166 | 430 | 774 | 760 | 720 | 637 | 3769 | |
| Fraction F | A | 29% | 20% | 38% | 34% | 33% | 33% | 33% | 30% | | |
| | B | 32% | 26% | 36% | 33% | 32 % | 34% | 35% | 31% | | |
| Fraction F+L | A | 34% | 23 % | 40 % | 37% | 40% | 45% | 41% | 38% | | |
| | B | 37% | 30% | 37 % | 38% | 39% | 48% | 45% | 39% | | |
| Sep. Ang. | | 1–43 | 44–88 | 88–132 | 132–175 | 180–141 | 141–99 | 99–57 | 57–30 | | |

3.2. Kinematic Properties of the CMEs

We ran the CORSET algorithm in all events in our list. So far it has tracked successfully 1101 out of 4262 COR2-A events (26%) and 646 out of 3769 COR2-B events (17%). Although this is a relatively small number of events, it still represents the largest sample of dual-viewpoint CME measurements and requires extensive analysis and discussion. To maintain a reasonable size and focus here, we chose to keep the kinematic analysis along with a discussion on the performance of the CORSET algorithm for a companion paper (L. A. Balmaceda et al. 2017, in preparation). In the following, we present a top-level summary of the kinematic measurements to (1) demonstrate that the supervised approach works and provides reliable measurements and (2) to show what data are available for each event.

There are several reasons for the low tracking success rate; lower signal-to-noise ratio in COR2-B compared to COR2-A; background levels varying as a function of solar cycle phase; and many faint events, especially in 2007–2010, etc. We had to intervene and customize the CORSET parameters often in order to increase the success rate, partially offsetting the advantages of the supervised approach. The final number of tracked events represents a compromise in maintaining a relatively automated measurement approach. We plan to fill in the measurements for the remaining events by manually delineating the CME contour in each image and letting the software used by CORSET to extract the kinematic and size parameters thus maintaining as close a correspondence to the automated measurements as possible.

In Table 3, we summarize the top-level statistics for the radial and expansion speeds (linear fits) and angular span per morphology type and telescope. The radial speeds are computed at the CPA. We discuss the results in Section 4.4.

Table 3
Average Properties of CMEs per Morphology Type Derived By the CORSET Algorithm for COR2-A and B

| Type | Events A/B | Radial Velocity (km s ⁻¹) | Expansion Velocity (km s ⁻¹) | Angular Span (Deg) |
|------|---------------|---|--|-----------------------|
| F | 506/312 | 389/439 | 344/395 | 54/50 |
| L | 136/97 | 733/747 | 929/903 | 86/75 |
| O | 301/166 | 416/495 | 311/343 | 39/37 |
| J | 55/20 | 340/444 | 117/122 | 15/13 |
| U | 75/33 | 329/450 | 132/232 | 25/19 |
| W | 28/18 | 182/265 | 128/160 | 33/35 |
| All | 1101/646 | 427/496 | 377/435 | 50/47 |

4. Discussion

The completed MVC catalog, free from the restrictions imposed by the single-viewpoint observations of the past, offers a fresh perspective of the properties of CMEs that can inspire many studies. Here, we discuss four obvious questions: What is the “true” CME rate? How does this catalog compare to other single-viewpoint catalogs? What do we learn about the CME morphology from the dual-viewpoint imaging?

4.1. Duty Cycle Corrections

To get a proper estimate of the CME occurrence rate, we first have to calculate the duty cycle of the COR2 telescopes. We follow the procedure outlined in Vourlidis et al. (2010). Similar approaches have been used by Howard et al. (1985) for *Solwind* and St. Cyr et al. (2015) for *Solar Maximum Mission (SMM)* and Mauna Loa Solar Observatory Mark III (Mk3) K-coronameter observations. The calculation of the duty cycle involves several steps and assumptions. The detection of a CME depends on its speed, given the observing cadence.

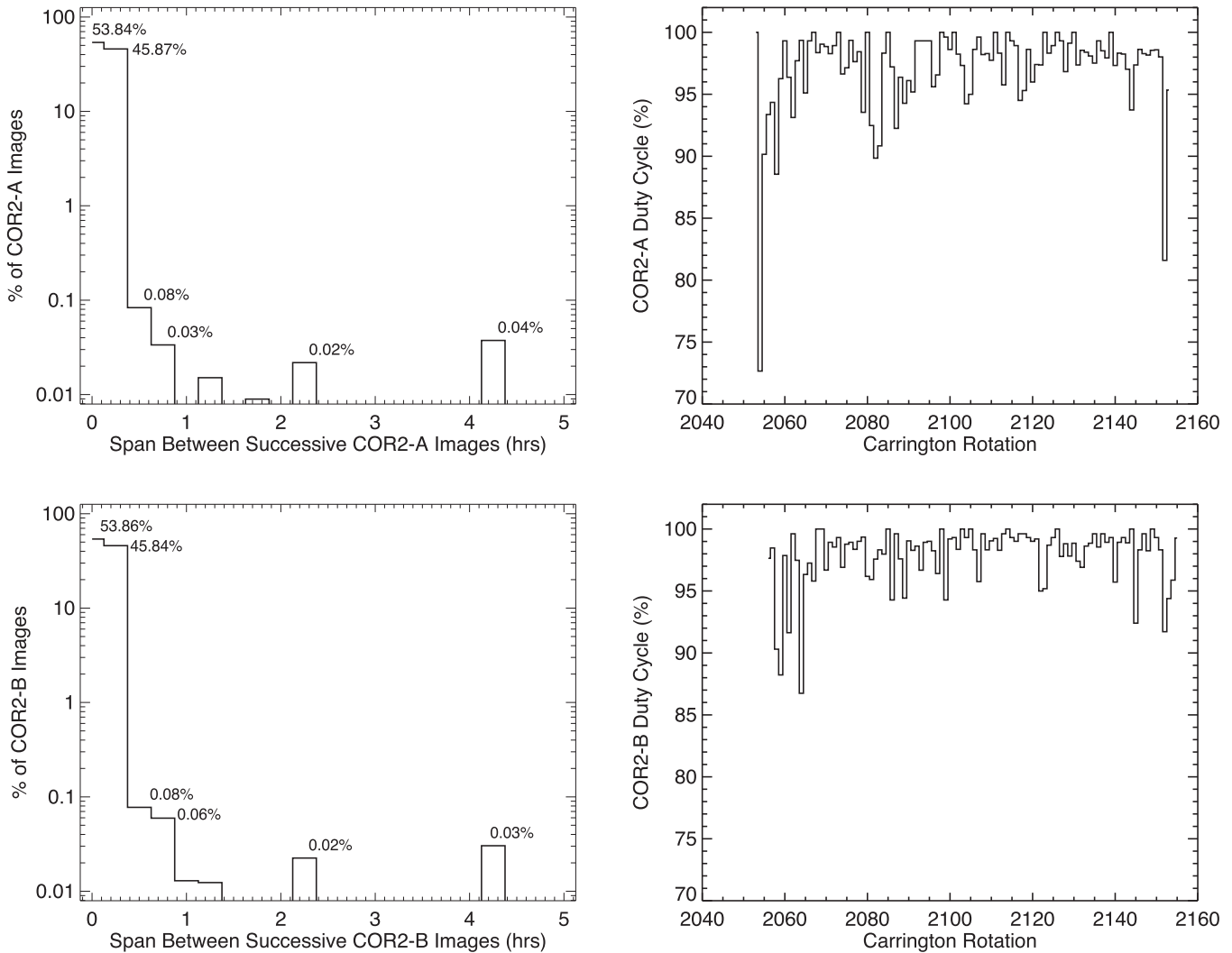


Figure 3. Duty cycle metrics for COR2-A (top panels) and COR2-B (bottom panels). Left: histogram of time spans between successive COR2 total brightness images (COR2-A: 3/2007-9/2014, COR2-B: 5/2007-9/2014) with the percentage of the most common cadences shown. 99.8% of all COR2 images were obtained at ≤ 30 min cadence, sufficient to capture a 3000 km s^{-1} CME. Right: average duty cycle per Carrington rotation considering all time gaps ≥ 2.4 hr, sufficient to obtain at least two images for CMEs $\leq 500 \text{ km s}^{-1}$.

Usually, a single image may suffice but two images are necessary to decide if it is a propagating event (a CME) and not an artifact. The second assumption regards the maximum speed for the event we desire to detect. The CME occurrence rate drops sharply as their speeds increase. For example, only 10 CMES, faster than 2500 km s^{-1} , exist in the whole of Cycle 23. The calculation of a daily rate does not make much sense for such rare events. Past practice considers instead an average CME speed for the duty cycle estimation. In our case, we adopt a typical CME speed of 500 km s^{-1} , which is about the average of our measured CMES for all event types across both COR2 telescopes (Table 3). This value is very similar to the speed used by Howard et al. (1985; 470 km s^{-1}). A 500 km s^{-1} CME will cross the $15 R_{\odot}$ COR2 FOV in 4.8 hr. Therefore, the maximum allowable gap between two successive COR2 images is 2.4 hr. Longer time gaps will affect the detectability of CMES $> 500 \text{ km s}^{-1}$ and hence will lower the duty cycle.

Similarly to the LASCO C3 duty cycle estimates (Vourlidis et al. 2010), we calculate two types of duty cycles (Figure 3). The first is a “mission” duty cycle that, as a single number, reflects the COR2 duty cycle for the duration of the mission (2007–2014, in this case). The number is derived from the

histogram of COR2 cadences shown in the left panels in Figure 3. We find that 99.7% of all COR2 images (both A and B) are taken within 30 minutes of each other. This cadence is sufficient for capturing two images of a 3000 km s^{-1} CME, which is close to the maximum CME speed ever measured (3380 km s^{-1}). Therefore, we can safely assume that all CMES will be detected with a 30 minute COR2 cadence. Hence, the COR2 duty cycle is 99.8%.

The second type of duty cycle is the average duty cycle per Carrington rotation, which is used to correct the CME daily rates, also calculated as Carrington rotation averages below. This duty cycle is calculated by totaling the time of all gaps > 2.4 hr within a Carrington rotation and dividing by the hours in the rotation. The results are shown in the right panels of Figure 3. Note that our COR2-A values start in 2007 March, while COR2-B starts in 2007 May and the large gap (~ 6 days in mid-March) is absent in the COR2-B plot. The drop in COR2-A cadence after rotation 2150 (2014 July–September) corresponds to the reduction of the *STEREO-A* telemetry due to the switch to side-lobe antenna operations as the spacecraft approached opposition. A similar switch was planned for COR2-B but communication was lost before it was

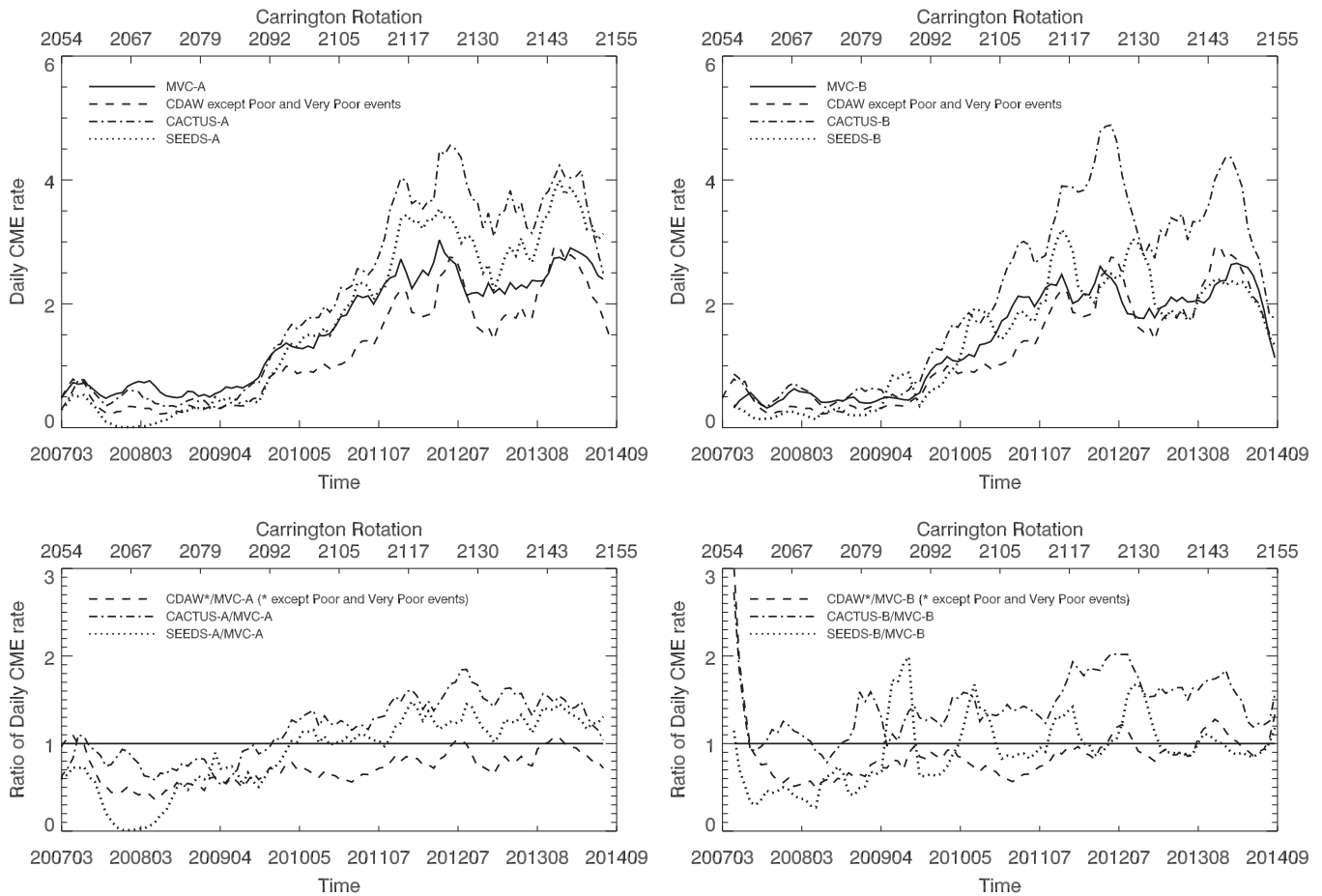


Figure 4. Top panels: comparison of daily CME rates between the MVC catalog and the rates from the CACTus, SEEDS, and LASCO CDAW catalogs. The rates are averaged over a Carrington rotation, smoothed by a five-point window, and corrected for duty cycle (see Section 4.1). The rates for COR2-A are on the left and for COR2-B on the right panels. The CDAW rates are from LASCO and hence are the same on both panels. Bottom panels: ratio of the rates in the other catalogs to the rates in this work.

implemented. Apart from these occasional drops in coverage, the rest of the COR2 duty cycle remains above 90% for the duration of the mission.

4.2. Comparison with Single-viewpoint Catalogs

Besides our catalog, we are aware of two more catalogs with COR2 CMEs list extending over the 2007 to 2014 time period. They are the CACTus and SEEDS catalogs, both relying on automated detection and property measurements. Of the two, only the SEEDS COR2 catalog attempts to cross-link events between its COR2-A and B lists but there are no details online as to how this is accomplished. The cross-links do not seem to be robust and we are not going to discuss them here. We are only going to compare the catalog as single-viewpoint catalogs. We apply the same duty cycle correction (Figure 3) to all three catalogs. For completeness, and because the LASCO CDAW catalog is used often by the community, we also compare the CDAW CME rates to the COR2 ones. To do that properly, we extended our LASCO duty cycle calculations from Vourlidas et al. (2010) to 2014 and recalculate it for a 500 km s^{-1} CME (LASCO C3 time gap of 5.4 hr). Following Wang & Colaninno (2014), we remove from consideration the “Poor” and “Very Poor” Events” and apply the duty cycle correction to the remaining ones. Also, we excluded all SEEDS events with less than four frames.

In the top panels of Figure 4, we compare the COR2-A (left panel) and COR2-B (right panel) daily rates, calculated as averages over a Carrington rotation, smoothed by a five-point running mean window. The bottom panels display the ratios of the rates in the other catalogs over the rates in our list to facilitate the comparison among the various catalogs. The results are generally as we expected. The catalogs based on manual CME identification (CDAW and MVC) have similar CME rates across the solar cycle, though the CDAW rates are lower during the minimum and early rise phases. This is likely due to the exclusion of the “Poor/Very Poor Events” from the statistics. Several of these events must be true CMEs but we have no easy way of picking them apart from the other questionable detections in this category (see the discussion in Wang & Colaninno 2014). The ratio between the CACTus-A or SEEDS-A over the MVC-A rates varies significantly with the solar cycle, being close to 0.5, or even 0 for SEEDS-A, in solar minimum and rising to almost 2 during maximum. The situation is similar for the COR2-B rates, with the exception of the presence of large spikes in the SEEDS-B detection rates (Figure 4, bottom right). The first spike is most likely associated with the increase in the COR2 cadence of total brightness images (so-called “double” images in the observing program) in 2009 August (Carrington rotation 2087). As discussed previously (Wang & Colaninno 2014; Hess & Colaninno 2017), the CACTus, SEEDS, and CDAW catalog

statistics are affected by the cadence of the observations. Some of the other spikes seem to be correlated with temporary increases of the COR2 cadence but why are they only visible in the COR2-B statistics and not in COR2-A is not obvious to us and may warrant a separate investigation. Detection rates can also rise as solar activity picks up because the automated algorithms may get confused with the increased coronal outflows. The automated catalogs under-report CMEs during minimum because the events tend to be faint and thus are harder to detect. This is particularly obvious for SEEDS-A. SEEDS-B performs very similarly to the manual catalogs. Obviously, an automated detection algorithm requires fine-tuning for the given instrument and solar cycle phase (which modifies the coronal background). Since a variable threshold alters the detection statistics, comparisons across different catalogs and even analyses within the same catalog but over long time ranges are fraught with difficulties. We conclude that an experienced observer needs to be in the loop. Either the CME detections are done manually or the output of an automated detection procedure is vetted by a human.

4.2.1. Undetected CMEs—Visibility Function

Because of the intrinsic faintness of CMEs propagating out of the sky plane, there has always been a question on how many events are missed by coronagraphs, even for instruments with the high sensitivity and duty cycle of LASCO/C2. One expects that small, slowly expanding/propagating events, directed along the Sun-observer line will be hard to detect. Many halos are quite faint and constitute the hardest test for automated detection algorithms, for example. Pre-STEREO work on associations with low corona signatures and in situ shock/ICME detections suggested that 3%–7% of CMEs may go undetected (see Section 2.3 in Webb & Howard 2012), while Howard & Simnett (2008) found that as much as 15% of CMEs may have been missed by LASCO but detected in SMEI heliospheric imaging observations. They claimed that these events belonged to a new class of “mass-less” CMEs or “erupting magnetic structures.” The detection sensitivity of a coronagraph is usually referred to as its “visibility function,” and defined as the ratio of detected over total number of CMEs (e.g., Webb & Howard 1994, and references therein).

It was impossible to validate any of these results with observations from a single viewpoint since there is no other robust method for CME detection than white light coronagraph observations. Now we can address the issue of undetected CMEs because we have the simultaneous COR2 observations from two viewpoints and a catalog of CME events for each telescope. As noted in the beginning of Section 3, the COR2-A catalog has 4262 entries and the COR2-B has 3769 entries with 3358 events in common. This means that COR2-A has detected 704 CMEs that were not detected in COR2-B and COR2-B has 211 CMEs undetected in COR2-A. The distributions of the missing events relative to mission time and angular separation between the STEREO spacecraft are plotted in the top panel of Figure 5 and their statistics are shown in Table 4.

Of the missing events, 111 (16%) of “COR2-A”-only and 53 (25%) of “COR2-B”-only CMEs are due to data gaps in the other telescope (e.g., momentum dumps, on-board computer resets, intermittent downlink due to side-lobe operations) or pending analysis (i.e., 53 COR2-A events are from the March–April 2007 period not yet processed for COR2-B). As

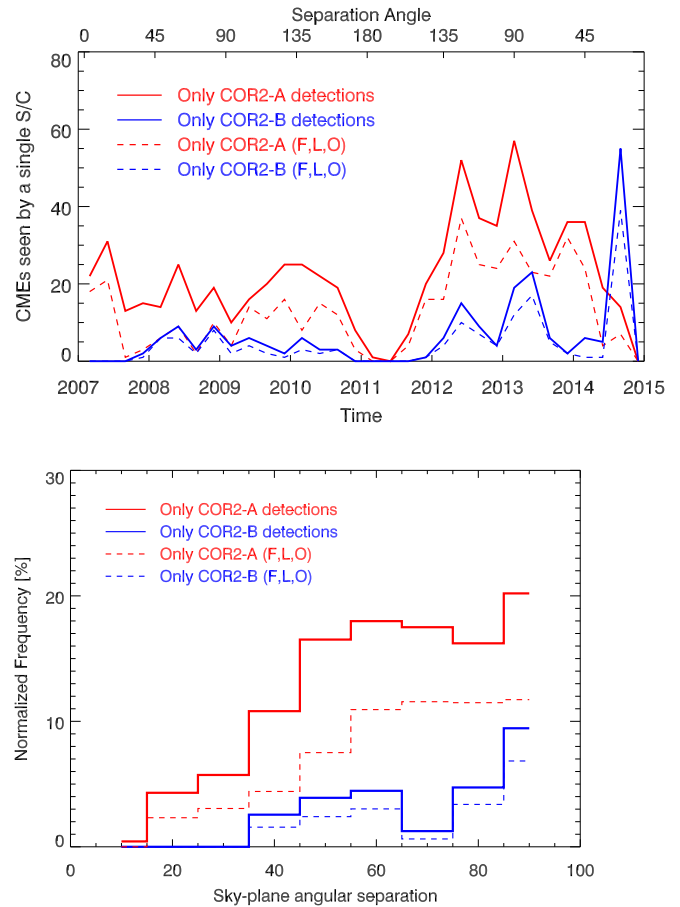


Figure 5. Top: three-month running average of CMEs detected by a single COR2 telescope. The bottom x-axis has the time and the top the angular separation between the telescopes. Bottom: histograms of the visibility function (missing CME rates) for the two coronagraphs as a function of angular distance from their perspective sky plane.

Table 4
Statistics of CMEs Detected in a Single COR2 Telescope and COR2 Visibility Functions

| Type | only in COR2-A | only in COR2-B |
|---------------------------|----------------|----------------|
| Total | 704 | 211 |
| Data Gaps | 111 | 53 |
| F | 113 | 49 |
| L | 5 | 3 |
| O | 214 | 55 |
| U | 86 | 24 |
| J | 111 | 19 |
| W | 64 | 8 |
| Missing CMEs | 593 | 158 |
| Rate (out of 4473 events) | COR2-B: 13.3% | COR2-A: 3.5% |

expected, there are very few missing CMEs in both telescopes in early 2011, when the STEREO spacecraft were in opposition and hence have the same line of sight.

This leaves 593 events in COR2-A and 158 events in COR2-B that went undetected in one of the COR2s even though the telescopes were operating normally. These events form the basis for calculating the visibility function for COR2-A/B. Uncovering the reasons for the event undetectability requires a

detailed study but we take a quick look at two issues: projection effects and event morphology.

The drop in the missing CME rate as the two spacecraft approach opposition (Figure 5, top) suggests that projection effects play a role. The peaks in the number of missing CMEs generally correlate with solar activity, especially the large increases in 2012 onward but there is also a “bump” in “COR2-A”-only detections in mid-2009 to 2010 when the *STEREO* spacecraft are in quadrature. To check whether Thomson scattering effects are at play, we bin the missing CMEs relative to the angular separation of each spacecraft from its sky plane. The angle is simply the spacecraft angular separation modulo 90° , and is 90° when the spacecraft are at exact quadrature. We use 10° bins and normalize the number of missing CMEs in each bin with the total number of unique events detected at that separation. This normalization removes the effect of solar cycle activity and provides the missing CME rate (the visibility function is 100% minus the missing rate) for each telescope. The results are plotted in the bottom panel of Figure 5, which reveals a rising trend in missing CME rates with increasing distance from the sky plane. The trend holds for both instruments despite the $\sim 4\times$ difference in rates between COR2-A and -B. We can draw two conclusions from this exercise: (1) CMEs start to appear differently in each telescope or equivalently, projection effects begin to matter, at about $30\text{--}40^\circ$ in angular separation. (2) The events missed are predominately events propagating along the coronagraph–Sun line. They may be halo or narrow CMEs. This is not altogether an unexpected result, but it demonstrates again the importance for Space Weather studies of observations off the Sun–Earth angle (and Section 4.3.3, also Vourlidas 2015).

To assess whether the CME morphology plays a role, we analyze the types of the missing CMEs. For COR2-A, 19% were “jets,” 11% were “waves,” and 14% were too faint to categorize (“unknown”). J-CMEs are, by our definition, narrow CMEs so they may have been occulted and/or too faint to see in COR2-B. The W-CMEs dim very quickly and U-CMEs are generally faint. Therefore, 44% of the missing events in COR2-B were likely too faint to be detected and corroborate the discussion above and the trend in Figure 5. The remaining 56% (332 events) were CMEs large enough to be detected. These events (the sum of F-, L-, and O-types) are plotted with dashed lines in both panels in Figure 5. Based on the comparison among the different curves, we deduce that the majority of missing COR2-B during the minimum (2008–2009) and a considerable fraction in 2009–2011 and mid-2012–mid-2013 are non-CME types (J, W, U). Looking closely at our notes for the other types, we find that 70 of them (35 F, 1 L, and 34 O) were likely faint, halo CMEs in COR2-B or could have been masked by another event in progress in the COR2-B FOV. We suspect that similar conditions hold for the remaining 262 events, but we cannot be certain without a thorough investigation, which is beyond the scope of this paper. Also, the non-CME types constitute an increased fraction of missed COR2-B CMEs as the spacecraft separation increases (as suggested by the divergence between the solid and dashed red curves in Figure 5, bottom). These findings are consistent with faint events and the low signal-to-noise ratio in COR2-B.

A similar analysis for the “COR2-B”-only events finds that 33% could have been easily missed in COR2-A (12% J, 5% W, and 16% U). The remaining 67% (107 events) are regular CMEs but 33 of them (19 F, 1 L, and 13 O) could have been

faint halos or overlapped with another event in COR2-A based on our notes for these events. We are left with 74 events for which the notes and keywords are incomplete so we will examine them along with the 262 events in COR2-A above.

In summary, our sample is large enough to allow a robust estimate of the visibility function for the two coronagraphs. We find that the COR2-A visibility function is 96.5% (3.5% missing rate) and the COR2-B is 86.7% (13.3% missing rate; Table 4). These numbers may look surprisingly close to the estimates from the LASCO era analyses quoted in the first paragraph. The higher rate of missing CMEs in COR2-B is due to the lower signal-to-noise ratio of the synoptic COR2-B total brightness observations because of the increased stray light background (Frazin et al. 2012).

4.3. CME Morphology from Different Viewpoints

Since the white light emission from the CME is optically thin, the morphological appearance of a given event depends strongly on the observer viewpoint. Our cross-linked catalog allows us to evaluate, with a large statistical sample, the role played by the viewpoint in the interpretation of CMEs. Are they all three-part CMEs? What is the true width of a CME? Are some (presumably narrow) CMEs missed when aimed directly along the Sun–observer line?

To appreciate the differences in the appearance of a CME from two viewpoints, we present some examples in Figure 6. The spacecraft separation for each event is shown on the right side of the figure. Clearly, the detection of a CME and the clarity of its substructures (front, cavity, prominence material, etc.) is more a projection effect rather than a reflection of the CME’s origin and/or source region properties (e.g., bottom two panels, Figure 6). The same CME exhibits a clear cavity (second row, left panel) in one view but lacks the cavity and reveals a wave on its flank (second row, right panel) in another view differing a mere 44° in its projection plane (the spacecraft are 136° apart). Although these examples were chosen to make a point, it did not take us long to locate them. The database contains plenty of events with similarly dramatic differences in morphology in simultaneous COR2-A and -B images. Figure 6 raises an important and somewhat worrisome issue. Many past studies (including our own) of CME morphology (and sizes) are subject to bias because they relied on single-viewpoint observations. The existence or not of cavities, prominences or shocks; the ratio of three-part CMEs; the true size of a CME; even the connection of a CME to its low corona origins based on feature identification, have all been analyzed and discussed in numerous papers and reviews and have been accepted by the community. However, their conclusions, we maintain, may be suspect and need to be reexamined and revised in view of the availability of two-viewpoint (and soon three-viewpoint) catalogs.

To this end, we examine the obvious question of whether projection effects are responsible for the relatively low percentage of FR-CMEs ($\sim 40\%$) in the statistics from single viewpoints (e.g., Table 1). Theoretical arguments suggest that all CMEs, or at least the grand majority of them, should contain flux ropes (Vourlidas 2014, and references therein). We focus on the events seen by both COR2s (3558 events). Table 5 shows the fractional distribution of all types in this sample. The letters indicate the morphological type (see Section 2.1). The rows show the COR2-A types and the columns show the COR2-B types.

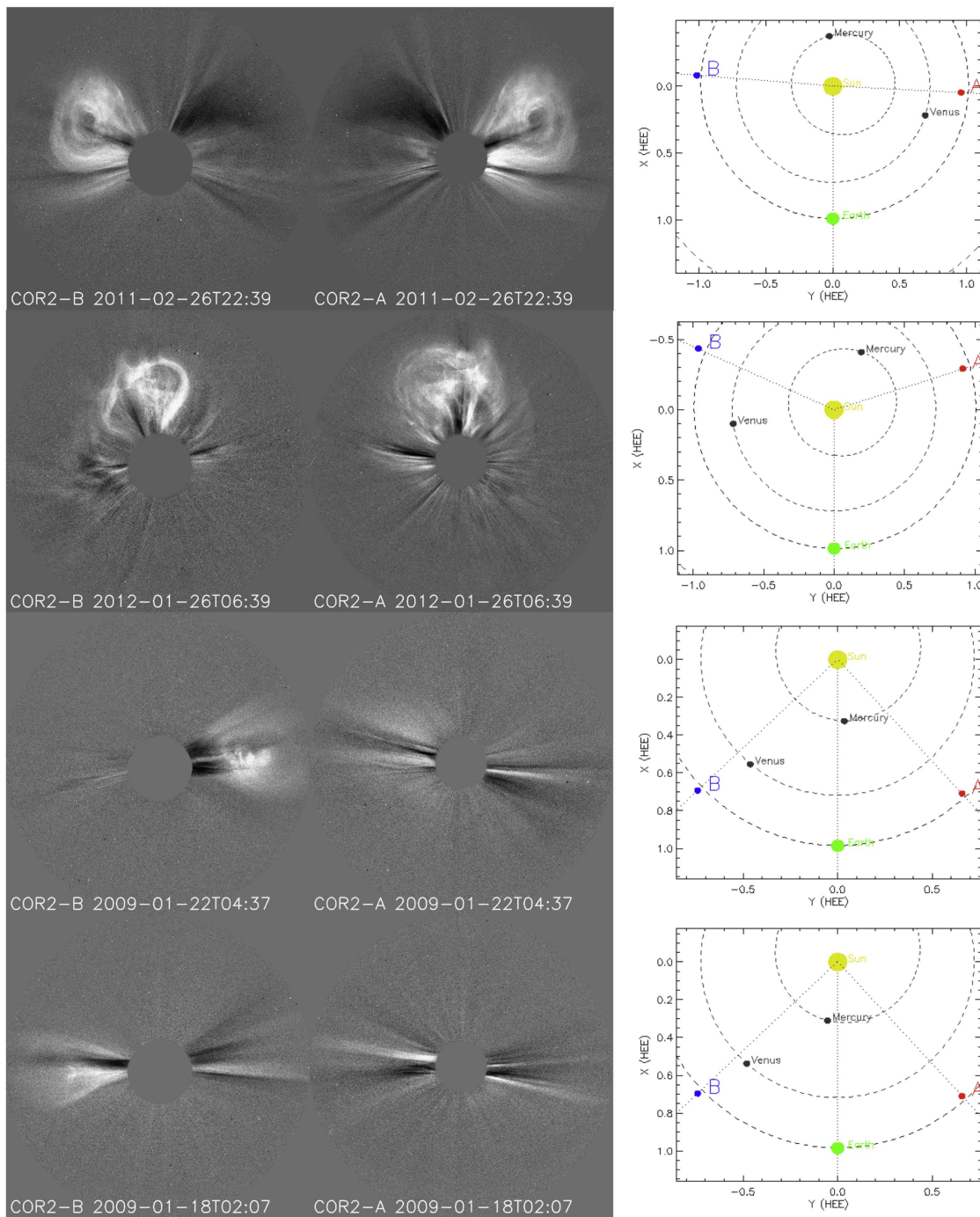


Figure 6. FR-CMEs exhibiting very different morphologies in simultaneous observations from two viewpoints. The viewpoint (spacecraft) separations are shown on the right side. Top row: FR-CME in both COR2-A and B. Second row: loop (A), flux-rope (B). Third row: outflow (A), flux-rope (B). Fourth row: undetected (A), flux-rope (B). The images are base differences of ratio images.

To obtain the total number of FR-CMEs, we sum the percentages of “F” and “L” types (rows and columns 1 and 3) and subtract the “F-F,” “L-L,” and “F-L” percentages once (because they are counted twice). The final percentage is 47.1% or 1582 FR-CMEs. When compared with the 39% in COR2-A, 41% in COR2-B, and 40% in LASCO (Vourlidas et al. 2013), we deduce that the inclusion of an additional viewpoint does increase the percentage of FR-CMEs by about 15%–20%, depending on the instrument. Therefore, projection effects play a partial role in the lack of flux-rope signatures for a given event. We expect that the addition of a third viewpoint (by

LASCO) and a formation of a three-viewpoint CME list (in progress) will increase the percentage of FR-CMEs by another ~20%, to ~55% of the events in the 2007–2014 period.

This is still not close enough to the theoretical expectation of 100% of CMEs, but we could consider a few potential corrections. First, the “W” types (2.9%) are not actual CMEs since they fail to escape into interplanetary space. They should not be considered in the statistics. Second, we argue that the J-CMEs (7.03%) should be included in the FR-CME category because they contain helical structures as both theory (Pariat et al. 2008) and observations (Patsourakos et al. 2008) suggest

Table 5
Fractional Distribution of CME According to Morphological Types Combining Two Viewpoints

| | | Type ST-B | | | | | | Total Fraction | Total Nr. of events |
|----------------|---|-----------|------|------|-------|-------|------|----------------|---------------------|
| | | F | J | L | O | U | W | | |
| Type ST-A | F | 28.19 | 0.06 | 2.42 | 3.54 | 0.22 | 0.14 | 34.57 | 1230 |
| | J | 0.03 | 6.63 | 0.03 | 0.25 | 0.20 | 0.03 | 7.17 | 255 |
| | L | 2.33 | 0.03 | 5.48 | 0.65 | 0.06 | 0.08 | 8.63 | 307 |
| | O | 2.19 | 0.37 | 0.62 | 30.69 | 0.59 | 0.31 | 34.77 | 1237 |
| | U | 0.20 | 0.31 | 0.08 | 0.39 | 10.26 | 0.28 | 11.52 | 410 |
| | W | 0.11 | 0.00 | 0.00 | 0.08 | 0.25 | 2.89 | 3.34 | 119 |
| Total Fraction | | 33.05 | 7.39 | 8.63 | 35.61 | 11.58 | 3.74 | 100 | |
| Events | | 1176 | 263 | 307 | 1267 | 412 | 133 | | 3558 |

(see also discussion in Vourlidas et al. 2013). Third, the “Unknown” CMEs could be FR-CMEs but the images are not clear enough to tell whether they are individual events or part of another event or even CMEs at all. We can also exclude those from the statistics. Applying these corrections, raises the potential percentage of FR-CMEs to 62.7% (1818/2899). Still, the flux-rope nature for a substantial number of CMEs—the 32% of the O-CMEs—remains unresolved.

4.3.1. What are the “Other” Events?

The lack of helical morphology for the O-CMEs can be due to many factors. They could originate as FR-CMEs, but their low corona evolution or the structure (or density) of the overlying arcades may disrupt or hide the flux rope. Hutton & Morgan (2015) used similar arguments to explain a similar percentage (30%) of CMEs associated with filaments eruptions but lacking clear three-part structure. They may contain multiple flux ropes resulting in a complex projection masking their flux-rope morphology. At least some of these events seem to be associated with $H\alpha$ or 304 Å surges that do not exhibit clear flux-rope morphologies (though they contain helical fields, see Vourlidas et al. 2003). Whether projection effects hide the flux-rope structure is an open question. The grand majority of these events appears as “O” in both COR2 viewpoints. The inclusion of the LASCO viewpoint will likely lower the number of “O” types, possibly by 20% as we argue above, but this still leaves a quarter of all CMEs between 2007 and 2014 as “Other.” The determination of the nature of these events requires a more detailed study.

As a final note, we point out the diagonal elements of Table 5. They show that an event of a given type is detected very frequently as such by both COR2s simultaneously. User bias may be present for some of these events. We identify and classify the events by looking at their time series on both telescopes simultaneously and even though we strive to classify each event in isolation, some bias may still be present in the classification of an event for one telescope based on its appearance on the other.

Another possibility is ecliptic symmetry. All coronagraph observations, be it from LASCO or SECCHI, are obtained from ecliptic viewpoints. As Hundhausen (1993) argued, CME locations follow the structure of the large-scale solar dipole. For example, CMEs appear at progressively higher latitudes as the dipole tilts toward the solar equator during maximum. They follow, in other words, the locations of the streamers. Consequently, CME observations over a full solar cycle are roughly equivalent to observations over the full range of ecliptic latitudes (0° – 90°). However, this argument also implies

that during a solar cycle phase, CMEs may exhibit a symmetry relative to the ecliptic. This situation is more readily evident during solar minimum, particularly the Cycle 22 minimum in 1996, when the solar dipole is aligned with the solar rotation axis and only one, equatorial streamer is present. In that case, CMEs are ejected in the ecliptic and their longitudinal properties will be hard to discern from ecliptic observations. It would be interesting to test this possibility with a detailed study of the sources and timing of the events that exhibit the same morphology in both COR2s.

4.3.2. Prominence Material

As part of the information collected during the catalog compilation, we report if an event shows the presence of a prominence (based on the appearance of filamentary structures) and $H\alpha$ material (based on very distinct signatures in the images, such as saturated pixels and extremely bright small-scale structures). We find that less than 1% of the CMEs in either COR2-A or -B show evidence for $H\alpha$ emission. They are 40 events in total, of which, 19 show bright emission in both COR2s, 16 only in COR2-A, and 5 only in COR2-B. For the case of prominence structures (but no obvious $H\alpha$ emission), we find roughly equal numbers in both telescopes: 1.6% (69 events) in COR2-A and 1.5% (55 events) in COR2-B. Events showing clear three-part morphology (traditionally associated with evidence of prominence eruption) sum to 1.85% (79) in COR2-A and 2% (75) in COR2-B.

In Figure 7, we show some cases in which the prominence can be clearly distinguished from only one of the viewpoints. The event in the top panel is a particularly impressive example. The filamentary structures, attributed to $H\alpha$ emission due to their excessive brightness, are seen only from COR2-A. The COR2-B images show only a rather diffuse halo with no indication of cool material in the corona. Statistics on prominence material in white light observations of CMEs are rare. We are aware of only the Howard et al. (1985) work who reported that about 1.5% of the CMEs during 1979–1981 showed such evidence for prominence material at approximately $4.0 R_\odot$. The COR2 statistics are in perfect agreement. Wood et al. (2016) found only two cases of cool material in CMEs deep in the inner heliosphere in all of the *STEREO* HI2 observations. Both works attributed the lack of $H\alpha$ signatures in the ionization of the material low in the corona. On the other hand, Lepri & Zurbuchen (2010) found that 4% of ICMEs measured at 1 au contained cool plasma, likely remnants of prominence material. Although this is a small percentage of all ICMEs, it is still three times higher than our and Howard et al.’s (1985) findings. Taking the prominence material statistics

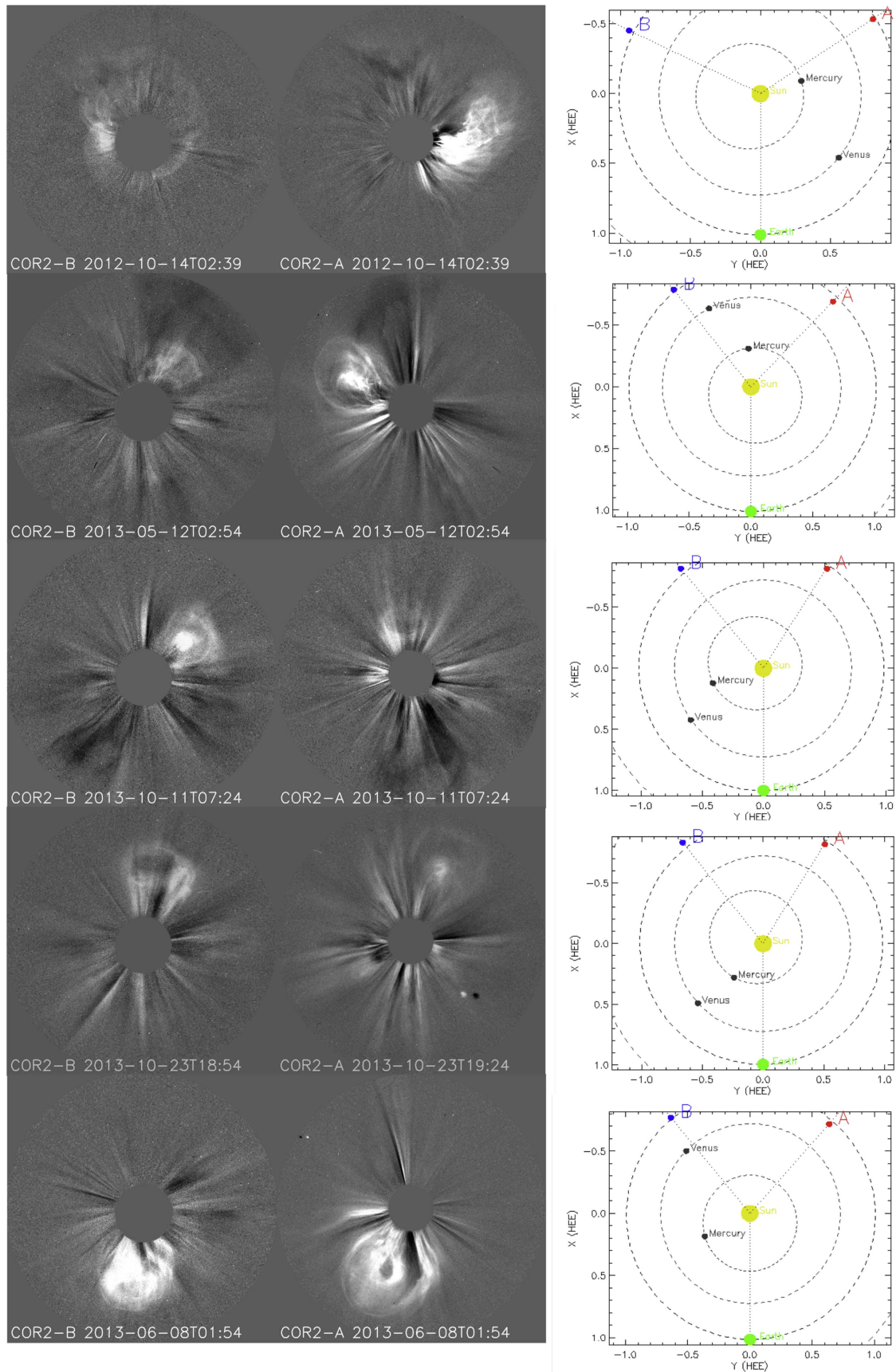


Figure 7. Examples of CMEs showing the presence of prominence material in one coronagraph view but not in the other. COR2-B (COR2-A) simultaneous images are on the left (right) and the relative locations of the *STEREO* spacecraft at the time of the observation are shown in the rightmost column. (From top to bottom) Panel 1: Likely H α material in COR2-A only. Panel 2: CME core with striations visible in COR2-A only. Panels 3-4: CMEs showing the same morphology from opposite COR2s demonstrate the commonality of CME morphologies and their projection dependence. Panel 5: Prominence material visible in COR2-A only.

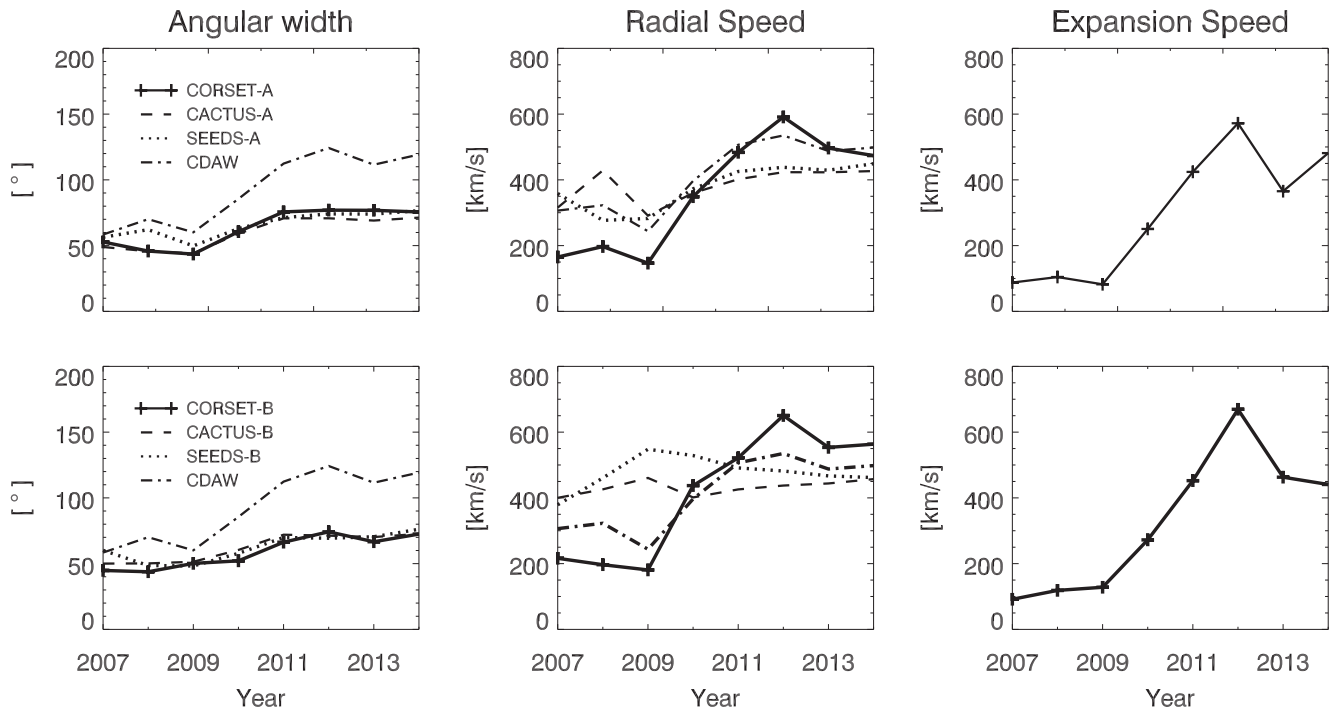


Figure 8. Yearly averages of select CME properties from different event catalogs for COR2-A (top) and -B (bottom). The catalogs are identified in the legends in the leftmost panels. The CDAW plots refer to LASCO measurements so the curves are the same in A and B panels. Left: CME Angular width. Middle: CME Radial speed. Right: CME Expansion speed. Only one curve is plotted because the MVC is the only catalog with this measurement.

into account only raised the percentage of cool material in the coronagraph images to 2.4%. This discrepancy could be explained if most of the cool material detected at 1 au was from ions other than hydrogen. For example, off-limb spectroscopy from the Ultraviolet Coronal Spectrometer (UVCS; Kohl et al. 1995) shows that about 38% of the events captured by UVCS had prominence material in Ly α emission (Giordano et al. 2013). The resolution and the proper investigation of the thermal evolution and composition of the ejected plasma from the low corona to Earth requires the deployment of off-limb spectroscopic capabilities in addition to white light coronagraphy (e.g., Kohl et al. 2006).

The remaining examples in Figure 7 demonstrate that the existence of a core, and to a lesser degree of a cavity, is a strong function of the viewpoint. Therefore, the absence of any of these characteristics in a CME does not mean anything for the origin or actual structure of the event. The core (and by extension a prominence) may very well be part of the event, but it cannot be detected because of the relative orientation of the event to that viewpoint. Proper statistics require at least two viewpoints.

4.3.3. Implications for Space Weather Studies

We have discussed, at great length, the influence of the observer viewpoint on the detectability and interpretation of CMEs. For those interested in the propagation and geo-effectiveness of CMEs, in particular, the projection effects on CME width, speed, and structure should give pause. Most, if not all, of the CME propagation models require the CME width and speed at around $20 R_{\odot}$ as input parameters. However, as the bottom two examples in Figure 6 attest, the CMEs may not even be visible from a particular viewpoint. There are obvious implications for space weather research and operations, if that

viewpoint is the Sun–Earth line. The reliance of space weather work on LASCO observations for the last 20 years may have made us complacent on the value of those measurements. The off-angle SECCHI observations show clearly, in our view, that a single viewpoint may not provide reliable measurements of CME properties.

It is true that slow and/or faint events will be the ones most affected by projection. From a space weather perspective, the large, bright CMEs should be clearly seen from LASCO or any other coronagraph along the Sun–Earth line. However, there is no guarantee that either the true extent or the actual structure of the magnetic flux rope heading to Earth will be visible as Figures 6 and 7 demonstrate. However, even slow events may be a concern if they are undetected. They will not be included in the operational models but they can interact with other CMEs, affect their properties, or become themselves geo-effective. The twin CMEs of 2012 March 7 offer a case in point. Patsourakos et al. (2016) were able to identify the Earth-directed CME only thanks to the COR2-A viewpoint. The CME was not detectable in either COR2-B or LASCO images and so it was missed by other researchers resulting in erroneous interpretations. In a more extreme example, Colaninno & Vourlidas (2015) were able to reconstruct the sizes and speeds of three CMEs (one of them Earth-directed) appearing quasi-simultaneously in the COR2 FOV, only thanks to the availability of all three viewpoints (COR2-A, COR2-B, and LASCO). The Earth-directed CME would have been missed from LASCO because it was slow and its emission was obscured by the other non-Earth-directed event. As Table 4 and associated discussion points out, this is not an uncommon occurrence. The existence of “stealth” CMEs, visible only by off-angle viewpoints, is a concern for space weather as discussed by Robbrecht et al. (2009) and Lynch et al. (2016).

4.4. CME Properties

We defer the detailed analysis of the 1747 events where the application of the CORSET algorithm was successful for another paper (L. A. Balmaceda et al. 2017, in preparation). Here, we briefly discuss a few key parameters (radial and expansion speeds, and width) and compare them with the measurements in other catalogs. The expansion speed is a quantity unique to our catalog.

We plot yearly averages of these quantities from the three catalogs (CACTus, SEEDS, and LASCO CDAW) against our CORSET-derived measurements in Figure 8. To reduce the effect of outflows and other misidentifications in the automated catalogs, we ignore all events narrower than 20° from the statistics (Figure 8, top). All three COR2 catalogs report very similar angular widths and solar cycle variations. SEEDS-A seems to overestimate the widths during the deep minimum but the effect is small. The main discrepancy is between the COR2 and LASCO catalogs. The CDAW widths are consistently larger than the rest, especially during the maximum. This seems to imply a bias. CME shock and/or streamer deflections may have been included but these had to be faint in order to be missed by the other catalogs. Alternatively, the larger LASCO FOV ($32 R_\odot$) compared to the $15 R_\odot$ FOV of COR2 may play a role. Multiple CMEs, more common during maximum, tend to merge within the LASCO C3 FOV resulting in, presumably, wider events that may bias the statistics. However, the $2\times$ difference between CDAW and the other catalogs needs further investigation.

The radial (projected) speeds show a larger spread among the catalogs (Figure 8, middle) but similar solar cycle behavior. FOR COR2-A measurements, CDAW and CORSET agree and show a strong increase in speeds in 2010. The automated catalog agree between them and show a much softer rise. In COR2-B, things are different. In particular, SEEDS-B, and to a lesser degree CACTus-B, show the opposite behavior than CORSET, CDAW, and COR2-A. They show speeds increasing in 2009 and diminishing toward maximum. This is clearly discrepant based on the other measurements and what we expect (and know) for solar maximum CMEs. We will not attempt to interpret the underlying issues here and consider the SEEDS and CACTus speeds for COR2-B, unreliable prior to 2010, at this point. There is a similar effect for CACTus-A in 2008. CORSET speeds during minimum are the lowest of the group in both COR2s. This is likely due to CORSET performing better for slower moving CMEs and we will explore it more in the next paper.

Finally, we have no statistics on CME expansion speeds from other catalogs. The CORSET results follow the radial speed pattern, with low expansion speeds during minimum and a rapid increase from 2010 to 2012 by almost a factor of six. We note that these speeds refer to the total expansion—the rate of change of the distance between the CME flanks—and need to be divided by two if the expansion speed relative to the center of mass is desired. The increase in 2014 may or may not be real given the partial coverage of that year in our sample. However, it is consistent with the two-peaked cycle seen in sunspot numbers and noted in CMEs by other researchers (e.g., Wang & Colaninno 2014).

Overall, the supervised approach using the CORSET algorithm is encouraging. It allowed us to extract a large sample of kinematic and geometric measurements from our CMES and the measurements are in good agreement with other catalogs. Of course, there

are differences and we have not analyzed the large number of two-viewpoint measurements. These should provide a wealth of new information on CMEs and on the reliability of previous single-viewpoint analyses. The results will be reported soon in L. A. Balmaceda et al. (2017, in preparation).

5. Conclusions

We have compiled a database of 8031 CMEs detected from the two viewpoints of the COR2-A and -B coronagraphs called the MVC catalog. A supervised image processing algorithm provided automated extraction of key CME properties, such as radial and expansion speeds, CPA, and width, for 20% of the events. In addition, we assess the morphology of each event and categorized it within a set of physically motivated types. This is the most comprehensive effort, to date, to characterize, cross-link, and extract properties of a CME event from two viewpoints. The catalog and individual CME measurements are publicly available through the web page of the JHUAPL solar section (solar.jhuapl.edu). The findings and discussion in the present paper can be summarized as follows.

1. We identified 4473 unique CME events from March (May for COR2-B) 2007 to September 2014 with 3358 (75% of total) detected in both COR2s. We have extracted, semi-automatically, kinetic and geometrical properties for 1747 of the events.
2. There are 4262 events in COR2-A and 3769 in COR2-B. The differences are largely attributed to data gaps in one of the telescopes. However, we have found 593 (158) events that could not be detected in COR2-A (COR2-B) even though the instrument was observing at the time. Many of them could have been missed because they were faint and/or narrow (e.g., jets, waves, unknown).
3. The CME visibility function for COR2-A is 96.5% and for COR2-B is 86.7%. The reason for the lower percentage in COR2-B is likely the increased stray-light background of the instrument resulting in a lower signal-to-noise ratio and thus a higher likelihood of missing faint events.
4. 47% of the CMEs, detected in both COR2s, exhibit signatures of flux-rope morphology. This percentage is higher than single-viewpoint statistics (i.e., 39% in COR2-A, 41% in COR2-B, 40% in LASCO) by about 15%. If we exclude non-CMEs and unknown events, the ratio of FR-CMEs rises to 63%.
5. We calculate the duty cycle of both COR2s. The mission duty cycle (2007–2014) is 99.7%, for CMEs of all speeds, and the average duty cycle per Carrington rotation is generally higher than 90%, for CMEs $\leq 500 \text{ km s}^{-1}$ (Figure 3).
6. We provide duty-cycle corrected daily CME rates (averaged over a Carrington rotation), and compare them with the rates from other COR2 and LASCO catalogs in Figure 4. The rates between the catalogs with manual CME identification (CDAW and MVC) are very similar while the catalogs based on automated detection report higher rates during maximum and lower rates during minimum (when CMEs are fainter) by as much as 60%. The performance of automated techniques varies at different phases of the cycle (e.g., CACTUS-B during solar minimum, SEEDS-A during the rise) reflecting the dependence of their detection rate on the thresholds used

for the particular instrument. Therefore, a technique fine-tuned for a particular coronagraph may not work as well for a different instrument. The necessary change in the threshold is then likely to affect the statistics.

7. The apparent CME morphology greatly depends on the observer viewpoint (Figure 6). Projection effects can hide/confuse important structures such as the core, cavity, or the extend of the shock. Therefore, skepticism is advised for studies and methodologies that rely on the analysis of CME structure to examine origin or physical attributes of CMEs.
8. We find that $<1\%$ of CMEs have partially ionized prominence material in the COR2 FOV in agreement with past results from *Solwind*. Also, only about 1.5% of the CMEs show clear evidence of filamentary material. We also find that $H\alpha$ emission or even filamentary structure is subject to projection effects and is not always visible in both telescopes (Figure 7).
9. 3% of the events in the catalog are not CMEs, though they look like CMEs in their first appearance in COR2. These events become faint and disappear before they reach the end of the FOV. These “failed” CMEs (Vourlidas et al. 2010) are likely waves launched by motions in the low corona.
10. Despite the availability of two viewpoints, there remain 370 events (about 30% of total) that are hard to classify. They do not have clear flux-rope morphologies, they do not fade in the COR2 FOV, and they are too wide to be jets. We believe that these are FR-CMEs whose structure is either masked by overlying coronal material piled up during the eruption or comprise multiple flux ropes or represent “broken” flux ropes (i.e., surges). However, these assertions and the nature of these events need to be assessed with a careful study.
11. We have extracted kinematic and geometric measurements for 1747 CMEs (1101 events in COR2-A and 646 in COR2-B). We find similar widths to other COR2 catalogs (CACTus, SEEDS). The LASCO CDAW widths, during maximum, are about $2\times$ larger than all of the other catalogs. CORSET tends to report lower speeds during minimum but that may be small sample bias. The COR2-B speeds from the automated catalogs (SEEDS, CACTus) are at odds with all of the other measurements (Figure 8, middle) and therefore are suspect. The CME expansion speeds, only available in the MVC catalog, follow the solar cycle showing a strong six-fold increase from 2010 to 2012. There is an indication that the expansion speeds follow the double-peaked behavior seen in sunspots with peaks in 2012 and 2014.

The database is still in development. In the near future, we will process the COR2-B observations from 2007 March–April to bring the two lists into common time range. We will begin the calculation of the kinematic and geometric properties for the remaining events using the same routines as CORSET but identifying the CME boundary manually. The catalog will be updated as we get those measurements in. In the medium term, we will be adding the COR1 file information for each event and then proceed to calculate the mass and energy for each CME as a function of time, as we have done for the LASCO CDAW list. At the same time, we will be adding the last remaining viewpoint, the LASCO C2 and C3 information as part of a

separately funded project. At the moment, we do not plan to extend the catalog beyond 2014 September unless COR2-B observations or appropriate funding become available.

A.V. was partially funded for this work by LWS under ROSES NNX13ZDA001N (NNX15AT42G) and by NASA grants NNX16AH70G and NNX17AC47G. L.A.B. was supported by FAPESP Projects 2014/23716-4 and 2013/03085-7 and wishes to thank JHUAPL for their hospitality during this fellowship. G.S. was supported by NASA contract S-13631-Y to NRL. A.D.L. thanks CNPq (grant 304209/2014-7). The CME list and APL Solar site are supported by NASA NNX16AH70G and APL internal funds. The SECCHI data are produced by an international consortium of the NRL, LMSA-L and NASA GSFC (USA), RAL and University of Birmingham (UK), MPS (Germany), CSL (Belgium), and IOTA and IAS (France). The LASCO CDAW CME catalog is generated and maintained at the CDAW Data Center by NASA and The Catholic University of America in cooperation with the Naval Research Laboratory. *SOHO* is a project of international cooperation between ESA and NASA.

References

- Alzate, N., & Morgan, H. 2016, *ApJ*, 823, 129
- Berghmans, D. 2002, in ESA Special Publication 506, Solar Variability: From Core to Outer Frontiers, ed. A. Wilson (Noordwijk: ESA Publications Division), 85
- Bonte, K., Jacobs, C., Robbrecht, E., et al. 2011, *SoPh*, 270, 253
- Bosman, E., Bothmer, V., Nistic, G., et al. 2012, *SoPh*, 281, 167
- Boursier, Y., Lamy, P., Llebaria, A., Goudail, F., & Robelus, S. 2009, *SoPh*, 257, 125
- Boursier, Y., Llebaria, A., Goudail, F., Lamy, P., & Robelus, S. 2005, *Proc. SPIE*, 5901, 13
- Braga, C. R., Dal Lago, A., & Stenborg, G. 2013, *AdSpR*, 51, 1949
- Brueckner, G. E., Howard, R. A., Koomen, M. J., et al. 1995, *SoPh*, 162, 357
- Burkepile, J. T., Hundhausen, A. J., Stanger, A. L., St. Cyr, O. C., & Seiden, J. A. 2004, *JGRA*, 109, A03103
- Byrne, J. P., Morgan, H., Habbal, S. R., & Gallagher, P. T. 2012, *ApJ*, 752, 145
- Colaninno, R. C., & Vourlidas, A. 2015, *ApJ*, 815, 70
- Cremades, H., & Bothmer, V. 2004, *A&A*, 422, 307
- Domingo, V., Fleck, B., & Poland, A. I. 1995, *SoPh*, 162, 1
- Floyd, O., Lamy, P., Boursier, Y., & Llebaria, A. 2013, *SoPh*, 288, 269
- Frazin, R. A., Vsquez, A. M., Thompson, W. T., et al. 2012, *SoPh*, 280, 273
- Giordano, S., Ciaravella, A., Raymond, J. c., Ko, Y.-K., & Suleiman, R. 2013, *JGR*, 118, 967
- Gopalswamy, N., Yashiro, S., Michalek, G., et al. 2009, *EM&P*, 104, 295
- Gopalswamy, N., Yashiro, S., Michalek, G., et al. 2010, *SunGe*, 5, 7
- Goussies, N., Stenborg, G., Vourlidas, A., & Howard, R. 2010, *SoPh*, 262, 481
- Hess, P., & Colaninno, R. C. 2017, *ApJ*, 836, 134
- Howard, R. A., Moses, J. D., Vourlidas, A., et al. 2008, *SSRv*, 136, 67
- Howard, R. A., Sheeley, N. R., Michels, D. J., et al. 1985, *JGR*, 90, 8173
- Howard, T. A., & Simnett, G. M. 2008, *JGR*, 113, A08102
- Hundhausen, A. J. 1993, *JGR*, 98, 13177
- Hutton, J., & Morgan, H. 2015, *ApJ*, 813, 35
- Hutton, J., & Morgan, H. 2017, *A&A*, 599, A68
- Kaiser, M. L., Kucera, T. A., Davila, J. M., et al. 2008, *SSRv*, 136, 5
- Kohl, J. L., Esser, R., Gardner, L. D., et al. 1995, *SoPh*, 162, 313
- Kohl, J. L., Noci, G., Cranmer, S. R., & Raymond, J. C. 2006, *A&ARv*, 13, 31
- Kwon, R.-Y., Zhang, J., & Vourlidas, A. 2015, *ApJL*, 799, L29
- Lepri, S. T., & Zurbuchen, T. H. 2010, *ApJL*, 723, L22
- Lynch, B. J., Masson, S., Li, Y., et al. 2016, *JGR*, 121, 10677
- Olmedo, O., Zhang, J., Wechsler, H., Poland, A., & Borne, K. 2008, *SoPh*, 248, 485
- Pariat, E., Antiochos, S. K., & DeVore, C. R. 2008, *ApJ*, 691, 61
- Patsourakos, S., Georgoulis, M. K., Vourlidas, A., et al. 2016, *ApJ*, 817, 14
- Patsourakos, S., Pariat, E., Vourlidas, A., et al. 2008, *ApJL*, 680, L73
- Robbrecht, E., & Berghmans, D. 2004, *A&A*, 425, 1097
- Robbrecht, E., Berghmans, D., & Van der Linden, R. A. M. 2009, *ApJ*, 691, 1222
- Shen, C., Wang, Y., Pan, Z., et al. 2013, *JGR*, 118, 6858

- St. Cyr, O. C., Flint, Q. A., Xie, H., et al. 2015, [SoPh](#), **290**, 2951
- Temmer, M., Preiss, S., & Veronig, A. 2009, [SoPh](#), **256**, 183
- Thernisien, A. 2011, [ApJS](#), **194**, 33
- Vourlidas, A. 2014, [PPCF](#), **56**, 64001
- Vourlidas, A. 2015, [SpWea](#), **13**, 197
- Vourlidas, A., Howard, R. A., Esfandiari, E., et al. 2010, [ApJ](#), **722**, 1522
- Vourlidas, A., Lynch, B. J., Howard, R. A., & Li, Y. 2013, [SoPh](#), **284**, 179
- Vourlidas, A., Wu, S. T., Wang, A. H., Subramanian, P., & Howard, R. A. 2003, [ApJ](#), **598**, 1392
- Wang, Y.-M., & Colaninno, R. 2014, [ApJL](#), **784**, L27
- Webb, D. F., & Howard, R. A. 1994, [JGR](#), **99**, 4201
- Webb, D. F., & Howard, T. A. 2012, [LRSP](#), **9**, 3
- Wood, B. E., Howard, R. A., & Linton, M. G. 2016, [ApJ](#), **816**, 67
- Yashiro, S., Gopalswamy, N., Michalek, G., et al. 2004, [JGRA](#), **109**, A07105